ELSEVIER

Materials Science and Engineering A276 (2000) 133–140

MATERIALS SCIENCE & ENGINEERING A

www.elsevier.com/locate/msea

Formation of carbides by electro-discharge machining of alpha iron

E.D. Cabanillas [a], J. Desimoni [b], G. Punte [b], R.C. Mercader [b,*]

[a] *Departamento de Materiales, Centro Atómico Constituyentes, Comisión Nacional de Energía Atómica, Avenida del Libertador 8250, 1429 Buenos Aires, Argentina*

[b] *Departamento de Flísica, Facultad de Ciencias Exactas, Universidad Nacional de La Plata, C.C. 67, 1900 La Plata, Argentina*

Received 22 March 1999; received in revised form 14 June 1999

Abstract

The surface of pure iron sheets have been submitted to spark-planing erosion using kerosene as dielectric under a wide range of machining conditions: discharge duration times between 2 and 3072 μs, and spark currents between 3.3 and 25 A. The carbides formed by the electro-discharge machining process have been identified by X-ray diffraction and Mössbauer spectroscopy. Two different regimes of carbide formation were established: for sparks of energy below ≈ 0.5 J only ε-carbide, austenite and martensite were observed; for sparks of higher energy mainly cementite, austenite and traces of martensite, Fe_7C_3, or Fe_5C_2 were detected.

Keywords: X-ray diffraction; Mössbauer spectroscopy; Electro-discharge machining; Carbide formation; Surface planing

1. Introduction

When pure iron samples immersed in kerosene are subjected to electro-discharge-machining, a layer composed of austenite, martensite and unidentified iron carbides is formed [1]. The nature of this covering has an important influence on the mechanical properties and wear resistance of the surface. Accordingly, the assessment of its composition and depth is necessary to control the properties of the surface of the tool or device in which the spark-planed material might be used. Through the modification of these variables it may be possible to tailor the characteristics of the surface and obtain the best properties toward a certain application without the need of any further handling.

Earlier studies of electro-discharge machining reported carbide formation by incorporation of carbon originated in the hydrocarbon dielectric cracking. For example, carbide formation was noted on the surfaces of pure titanium [2], uranium, and zirconium [3]. When electro-discharge machining is performed on steel surfaces, depending on the steel and machining conditions, a variety of microstructures can result [3–5]. The topmost recast layer formed by the resolidification of the molten material was found to be alloyed, at the bottom of the craters brought about by the sparks, with the pyrolysis products of the cracked hydrocarbon dielectric during the discharge [3]. For pure iron and ferrous alloys, this recast layer has been called 'white layer' because it has been found to be fairly resistant to etching by conventional metallographic reagents [6]. It has also been established that its microstructure for pure iron [6] and low carbon steels [7] samples consists of carbides in acicular or globular form distributed within an austenite matrix [8].

This work aims at adding to the knowledge of the parameters that influence the nature of the surface phases brought about by the spark-planing of pure iron samples. To that end, we have performed X-ray diffraction (XRD) and conversion electron Mössbauer spectroscopy (CEMS) studies, that have allowed us to identify and quantify different surface Fe-C phases induced by an electro-erosion process produced with rectangular pulses in a range of currents and discharge times.

* Corresponding author. Tel.: 54-21-424-6062; fax: +54-21-425-2006.

E-mail address: mercader@venus.fisica.unlp.edu.ar (R.C. Mercader)

0921-5093/00/$ - see front matter
PII: S0921-5093(99)00443-8

Table 1
Electric discharge parameters

Sample	Current (A)	t_0 (μs)	Energy (J)	Power (W)
S_A	3.3	2	0.00053	264
S_B	25	2	0.004	2000
S_C	25	16	0.032	2000
S_D	3.3	2048	0.541	264
S_E	3.3	3072	0.811	264
S_F	6.6	3072	1.622	528
S_G	13	2048	2.130	1040
S_H	13	3072	3.195	1040
S_I	25	3072	6.144	2000

2. Experimental

Iron metal sheets from Goodfellow Metals of 1.5 mm thickness, tempered quarter hard, 99.95 at.% purity, of composition Mn ≈ 3000; Si ≈ 1000; C < 800; P < 400; and S < 500 ppm, were mechanically cut into pieces of 25 × 25 mm [2]. Afterwards, the samples were spark-eroded in a commercial machine (CT Electromecánica, Ltd.®, Argentina), with the method of spark-planing devised by Cole [9]. The voltage between the tool and the sample was kept at 80 V. The duration of the discharge t_0 and its current i were chosen in the range: 2 μs ≤ t_0 ≤ 3072 μs, and 3.3 A ≤ i ≤ 25 A, see Table 1. The inactive time t_1 was set 9 t_0 for all samples (the period of the discharges was $t_0 + t_1$). The gap distance between tool and sample and the vertical feeding movement were servo-controlled. The rotating tool was built in copper with three grooves running radially to help remove debris. Tool and sample were both immersed in kerosene which was filtered and pumped to the gap from a reservoir.

The X-ray diffraction patterns were obtained at room temperature with a Philips PW1710 powder diffractometer, furnished with a diffracted beam graphite monochromator. Data were collected, using Cu-Kα radiation ($\lambda = 1.5406$ Å), in the range $15 \leq 2\theta \leq 125°$ at a step interval of 0.015° and a counting time of 8 s per step. The phases have been identified from searches in the PDF-2 [10] and Crystmet [11] databases. Rietveld line profile analyses have been used to characterize the treated surfaces. The refinements were performed using the program DBWS-9411 [12]. The sample displacement, the background (modeled with a fifth degree polynomial), the unit cell, the preferred orientation, the pseudo-Voigt profile parameters, the roughness of the surface and the scale factor of the different phases present in the sample were refined independently but not simultaneously. The starting models for the existing phases were taken from the Crystmet database [11]. From the Rietveld analysis a relative weight fraction was assigned to the refined phases. This approximation disregards the contributions of the minor phases, which could be recognized but not quantified and were therefore reported as traces. The accuracy in the phase abundance results was calculated from the scale factors and volume estimated standard deviations.

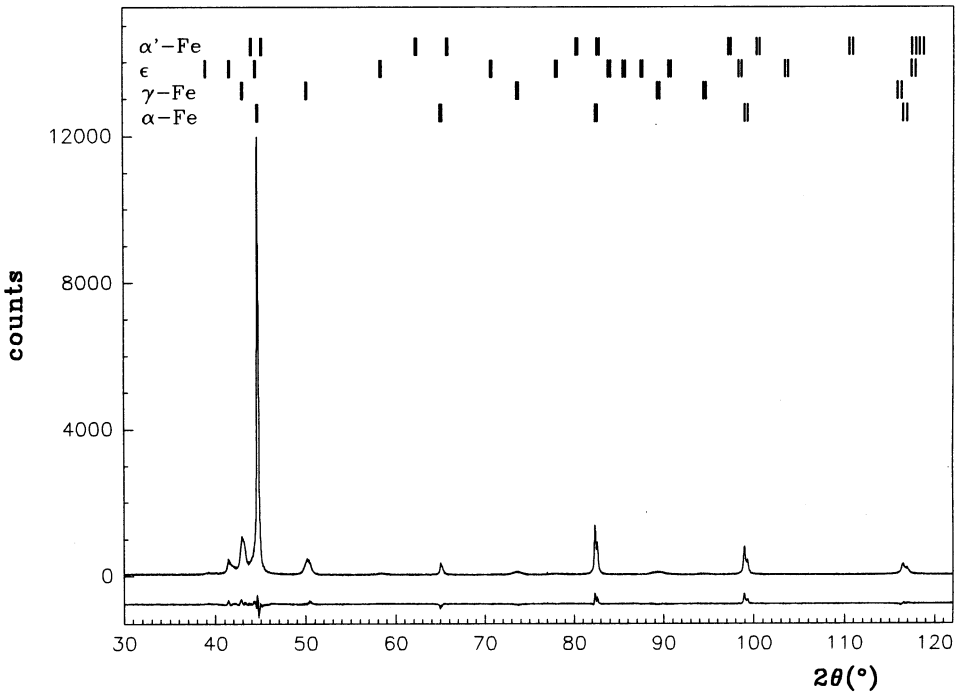

Fig. 1. X-ray diffraction pattern of α-Fe surface electro-discharge machined with 25A, 2 μs sparks. The data at the bottom are the differences between the experimental and Rietveld calculated intensities. The bars at the top show the positions of the diffraction lines of the indicated phases.

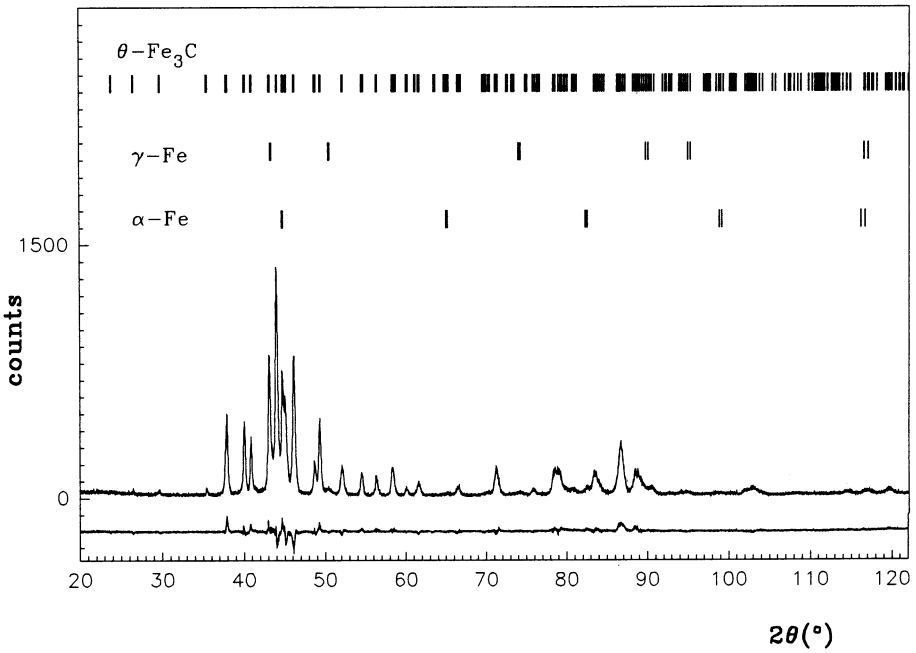

Fig. 2. X-ray diffraction pattern of α-Fe surface electro-discharge machined with 3.3 A, 3072 μs discharges. The line at the bottom shows the difference between experiment and Rietveld profile analysis calculated intensities. The bars at the top show the positions of the diffraction lines of the indicated phases.

Table 2
Cell parameters *a*, *b*, and *c*, (Å), obtained from the Rietveld refinements (estimated errors are shown as subscripts)

		α-Fe ferrite	γ-Fe austenite	Fe_2C ε-carbide	θ-Fe_3C cementite	Fe_7C_3	α′-Fe martensite	χ-Fe_5C_2 (Hägg)
S_A	*a*	2.8662_3	3.6372_2	2.664_2	–	traces	2.838_4	–
	c			4.338_2			2.980_5	
S_B	*a*	2.8662_3	3.6330_2	2.667_7	–	–	2.846_3	–
	c			4.342_5			2.966_4	
S_C	*a*	2.8661_1	3.6277_3	2.711_8	–	–	2.845_2	–
	c			4.348_8			2.944_2	
S_D	*a*	2.870_2	3.626_2	–	5.075_{18}	traces	–	traces
	b				6.765			
	c				4.515_6			
S_E	*a*	2.869_6	3.631_1	–	5.077_{11}	traces	–	traces
	b				6.753			
	c				4.511_1			
S_F	*a*	2.870_3	3.613_2	–	5.072_3	traces	–	traces
	b				6.753_3			
	c				4.508_2			
S_G	*a*	2.872_3	3.629_2	–	5.074_2	traces	–	traces
	b				6.760_5			
	c				4.513_2			
S_H	*a*	2.861_3	3.623_2	–	5.044_3	–	traces	–
	b				6.737_6			
	c				4.506_8			
S_I	*a*	2.867_6	3.634_2	–	5.057_3	–	traces	–
	b				6.716_3			
	c				4.515_4			

The CEMS spectra were taken in a conventional constant acceleration spectrometer of 512 channels with a 15 mCi nominal activity ^{57}CoRh source. The conversion electron detector was of the constant flow type operating with a mixture of He (94%) and methane (6%). The data were fitted by a least-squares program that used Lorentzian line shapes with constraints to simulate the hyperfine interactions observed in the spectra. Isomer shifts (δ) are referred to α-Fe at room temperature.

3. Results and discussion

The examination of the XRD patterns allowed to identify the major phases present and classify the samples in two different sets: set I, that includes the samples S_A, S_B and S_C; and set II, that comprises all the other studied samples. Fig. 1 displays the pattern of sample S_B that is representative of set I. It shows the lines characteristic of austenite (γ-Fe) and of ε-carbide (Fe_2C), beside those of ferrite (α-Fe), and a small percentage of martensite (α'-Fe). Fig. 2 displays the pattern belonging to sample S_E, representative of set II. This complex pattern could be fitted allowing for the presence of lines belonging to cementite (θ-Fe_3C), α-Fe, γ-Fe and traces of Fe_7C_3, and χ-Fe_5C_2 (Hägg carbide).

The Rietveld analyses performed on the samples of set I allowed to study the evolution of the phases that had been previously identified. It was determined that a decline in the fraction of the ε-carbide is accompanied with an increment of martensite. These results are

Table 3
(a) Relative areas (%) of surface species determined by conversion electron Mössbauer spectroscopy; and (b) relative abundance (%) of iron species determined by Rietveld profile analysis of X-ray diffraction data (estimated errors in the least significant digits are shown as subscripts)

Samples		S_A	S_B	S_C	S_D	S_E	S_F	S_G	S_H	S_I
α-Fe	(a)	32_5	45_7	48_7	5_6	10_3	12_3	14_7	14_4	15_4
	(b)	49.9_5	51.9_5	55.1_5	10_4	10_4	11_5	8_4	17_4	27_4
γ-Fe	(a)	30_9	37_9	36_9	7_{12}	7_4	7_4	11_9	15_4	21_6
	(b)	42.4_5	43.3_5	37.4_5	13_4	14_4	12_4	23_5	36_5	57_4
Martensite	(a)	2_4	4_5	7_4	–	–	–	–	–	–
	(b)	1.5_4	1.9_5	5.9_4	–	–	–	–	–	–
ε-carbide	(a)	36_9	14_6	9_9	–	–	–	–	–	–
	(b)	6.2_5	2.8_5	1.6_5	–	–	–	–	–	–
Fe_xC ($2.3 \leq x \leq 3.5$)	(a)	–	–	–	88_{22}	83_6	80_6	75_{14}	70_6	63_6
	(b)	–	–	–	77_4	76_5	77_4	68_5	47_4	19_5

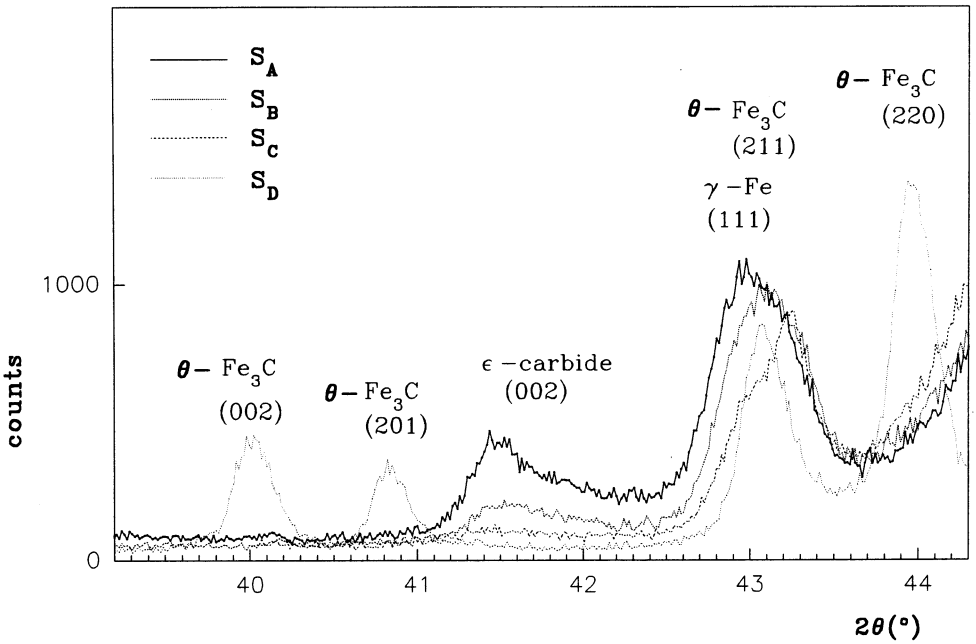

Fig. 3. zone of the X-ray diffraction patterns of samples S_A, S_B, S_C, and S_D to show the evolution of the more intense line of the ε-carbide.

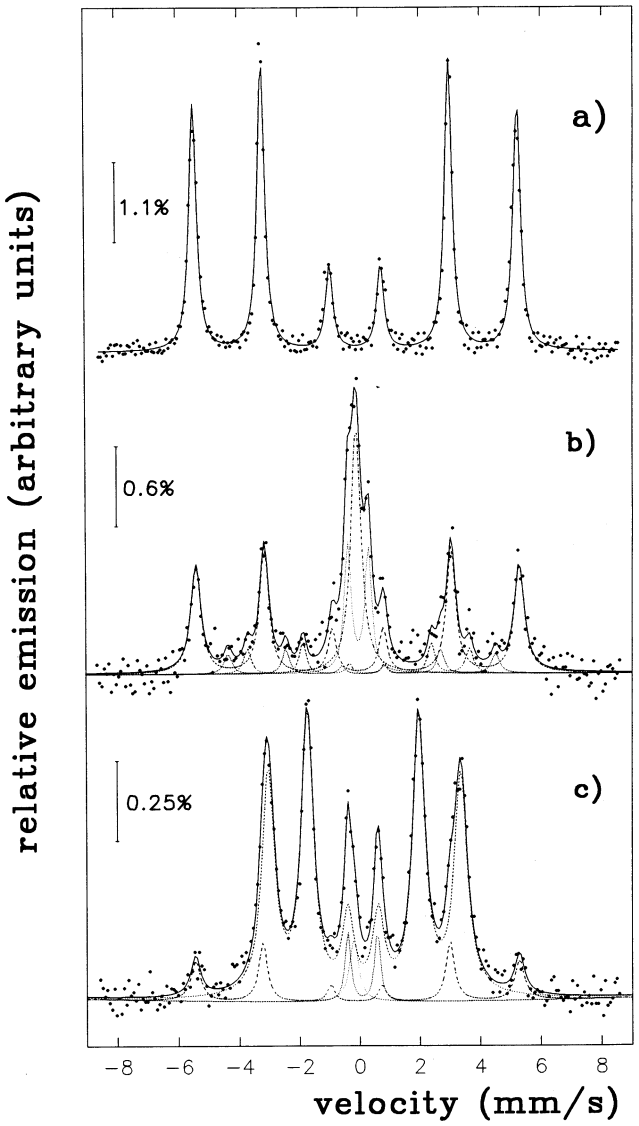

Fig. 4. CEMS spectra of (a) as received α-Fe; (b) electro-discharge-machined with sparks of 25 A and 2 μs; and (c) *idem* of 3.3 A and 3072 μs.

summarized in Tables 2 and 3. The number of phases present and the quality of the surfaces impaired a similar accuracy in the analyses of the XRD patterns of the samples of set II. In this set the cell parameters of only the main phases could be refined and just approximate percentages obtained. In addition, because small amounts of copper were observed on the surface of steel samples subjected to electro-discharge machining with copper electrodes [6,7], some copper may also exist on the surface of our pure iron samples treated in the same way. However, the positions of the XRD peaks of copper are coincident with those of austenite, and consequently the percentages of austenite determined through the Rietveld refinements may be somewhat overestimated.

Fig. 3 shows an augmented region of the XRD patterns that includes the most intense line, (002) of the ε-carbide, for samples S_A, S_B, and S_C of set I, and S_D, that belongs to set II. The data corresponding to S_D illustrates that the ε-carbide is absent for samples of set II.

The CEMS spectra of three selected samples are displayed in Fig. 4. Fig. 4(a) corresponds to the 'as received' sample. This spectrum shows the characteristic six lines belonging to the magnetic hyperfine field of pure α-Fe. Fig. 4(b) and (c) are the spectra of the samples labelled S_B and S_E, respectively; they are more complex than the spectrum of the untreated sample due to the simultaneous presence of a central peak belonging to paramagnetic austenite and of three different magnetic sextets that can be associated to ferrite, martensite and different carbides [13]. The six α-Fe magnetic lines displayed by the spectrum of sample S_B (Fig. 4b) are less intense than in the 'as received' sample. The possible assignment of the broadened sextets to other magnetic phases is discussed below. In Fig. 4(c) the α-Fe lines intensity is very small and the austenite signal has practically disappeared. The magnetic split spectra display lower field values than α-Fe and can be attributed only to carbides of several compositions [13].

The central peaks were assigned to austenite and simulated with a quadrupole doublet and one single line since the full complexity of the austenite Mössbauer spectrum (as suggested, e.g. by Génin [14]) is not resolved in this velocity range. This approximation, however, does not affect the relative subspectra areas. The hyperfine parameters after the fittings of all the studied samples are shown in Table 4 and the relative fractions (assuming equal recoilless factors for all phases) for the different samples are displayed in Table 3.

When signals arising from carbides of similar composition contribute to a total Mössbauer spectrum it is difficult to assign unambiguously the origin of each

Table 4
Hyperfine magnetic field, H, isomer shift, δ, quadrupole shift, 2ε, and quadrupole splitting, Δ, average values of the surface species determined by conversion electron Mössbauer spectroscopy (eimated errors are shown as subscripts and isomer shifts are referred to α-Fe at room temperature)

Species	H (T)	δ (mm/s)	2ε (mm/s)	Δ (mm/s)
α-Fe	33.0_1	0.02_2	0.00_1	
γ-Fe		-0.01_2 0.04_3		0.68_3
Martensite	26.6_4	-0.04_6	0.15_{18}	
ε-carbide	22_4	0.19_9	-0.04_7	
Fe_xC $(2.3 \leq x \leq 3.5)$	19.8_9	0.21_8	0.02_2	

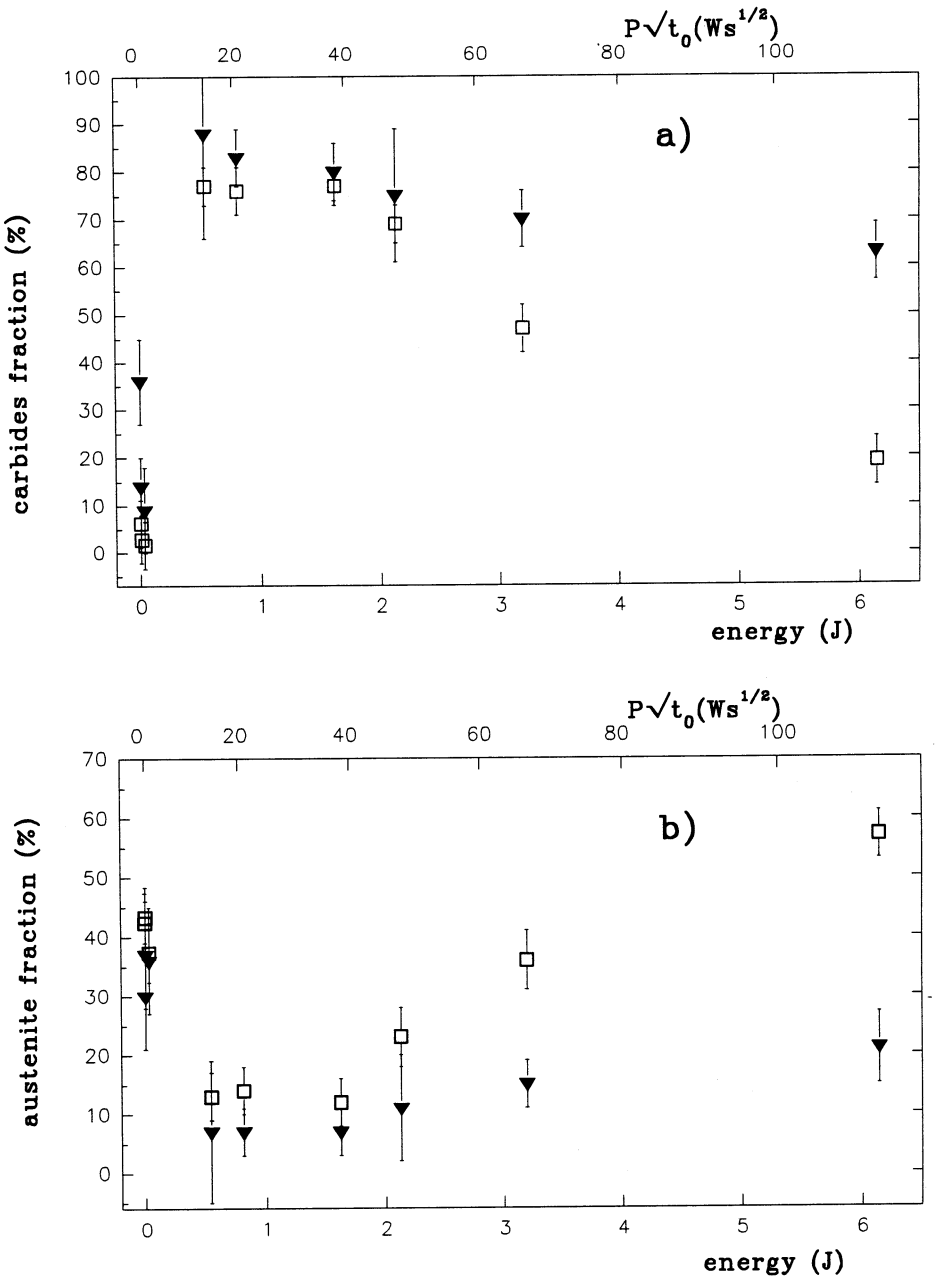

Fig. 5. (a) Carbides relative fractions determined by XRD, □, and CEMS, ▼, against discharge energy. (b) Austenite percentages determined by XRD, □, and CEMS, ▼, against discharge energy. The corresponding values of $Pt_0^{1/2}$ are shown on the top axis.

hyperfine field. The hyperfine field of 33T can be associated with Fe atoms without first near neighbor carbon atoms embedded both in a body centered cubic (bcc) or body centered tetragonal ferromagnetic environment. Environments of bcc structure are found both in ferrite (α-Fe) and in martensite (α'-Fe) of low carbon concentration. Therefore, when a signal of $\approx$ 27 T (that corresponds only to martensite [13]) is observed in a spectrum, iron probes without first neighbor carbon atoms belonging to this phase will also contribute partly to the intensity of the 33 T signal. This contribution will depend on the carbon concentration and its assignment will depend on the model used for the carbon distribution in the matrix. Therefore, although a small percentage of martensite is observed by XRD in samples S_A, S_B, and S_C, and traces in S_G and S_I, because the small contribution of iron atoms without near neighbor carbon atoms in martensite to the 33 T signal would be difficult to assess but would be only of minor intensity, we have assigned the 33 T sextets as belonging totally to α-Fe in Table 3.

The magnetic sextets of the CEMS spectra of set I were fitted with three different interactions to obtain good fittings. The first magnetic split interaction has a value of 33 T. The second magnetic component of set I samples ($H_{hf} \approx 20$ T) can belong to Fe_xC carbides with a wide range of compositions $2.3 \leq x \leq 3.5$ [14,15]. The hyperfine fields of this broad signal in our samples are coincident with those attributed to ε-carbide by Le Caer et al. [16] and Dubois and Le Caer [17]. Since ε-carbide is the only carbide observed by XRD in set I (with proportions that follow the same trend as the Mössbauer intensities) we assign this signal as arising only in probes belonging to ε-carbide. The carbon content increase observed in the ε-carbide detected on hot working die steel samples electro-sparked with an energy of about 6.4×10^{-3} J has been attributed previously to carbon incorporation from the cracked kerosene [18]. The third magnetic component of the CEMS spectra has a value of ca. 27 T and according to Ron [13] can be assigned only to martensite. Along the samples of set I this signal has a relative intensity that increases with the spark energy, in agreement with the XRD results. In the Mössbauer spectra of set II no 27 T signal is present. Since traces of martensite have been found through XRD in samples S_G and S_I, because the X-rays probe a deeper zone, we think this discrepancy is an evidence that the martensite formed in these samples lies at a greater depth than the range of the conversion electrons in iron (approx. 200 nm from the surface).

Set II contains a smaller percentage of austenite and different types of carbides. For this set, XRD results yield cementite, that was not present in the previous group, and traces of other carbides of compositions ranging from 2.33 to 2.5 Fe atoms per C atom that cannot be unambiguously quantified with the current data. The Mössbauer parameters (Table 4) of the signal attributed to carbides also have a range of variation within set II that reflects the different stoichiometries of these phases. Because of the very similar magnetic regimes and hyperfine parameters [13] and the poor statistics of the present data, it is unrealistic to elaborate a more detailed analysis of these findings.

Several theories have been proposed for the erosion mechanism [19,20]. A thermal origin for the ensuing phenomena after electro-sparking was considered [19] taking into account that the brief and intense current of ions flows in a narrow channel during a period of time that depends on the external electric circuit, generating locally an intense heat. Eubank et al. [21] assert that plasma is formed after the disruption, and, consequently, temperatures of about several thousand kelvins are attained. When the discharge ends, a resolidified layer of several micrometers deep (depending on the discharge parameters) is formed [3,22]. The surface is left covered with superimposed craters, pockmarks and chimneys [19].

Most models developed for temperature distributions that lead to the fusion of the surface [23–25] have a dependence on the transferred energy or on $Pt_0^{1/2}$, where P is the power and t_0 is the heating pulse duration. Hence, the dependence of the carbides and austenite fractions on energy and that on $Pt_0^{1/2}$ are shown in Fig. 5. The percentages of carbides obtained by CEMS and by XRD against the spark energy are displayed in Fig. 5(a). The percentage plotted includes carbides with different stoichiometries because no clear distinction can be found either between their X-ray patterns or between their hyperfine parameters. The CEMS spectra don't differ much from one species to the other, and because a Mössbauer spectrum is the superposition of the individual species, the total area is the sum of the unresolved subspectra that are comprised in it. Therefore, the ≈ 20 T signal is proportional to the total amount of carbides formed in the process. The proportion of austenite was also analyzed in this way, adding the contributions of the singlet and quadrupole split signals. The XRD and CEMS results are displayed in Fig. 5(b). Table 3 and Fig. 5 are consistent with the division of the samples in two sets suggested by the XRD and CEMS results. The spark energy of the set I samples never exceeds 0.5 J.

Iron carbides are generally formed in slow thermal processes where diffusion is involved [26], although some carbides have been reported to form in fast quenching of melted alloys and laser surface treatments [3,6,7,18]. The conditions of these experiments seem to be closer to the present situation because the rates of cooling of the melt pool in our samples, roughly calculated using the heat diffusion equation, range between 10^4 and 10^8 Ks^{-1}.

In our samples, no matter how fast the cooling rates are, there is a definite range in which some carbides are formed but not others. The formation mechanisms involved lead to the production of only austenite and ε-carbide when the energy is lower than 0.5 J. In particular, the production of ε-carbide must be due to a yet unknown non-equilibrium process. Other carbides are found to be formed when the energy of the sparks is higher (the higher the energy, the richer the carbon content in the composition of the carbide produced) and the contribution of the austenite subsides. The same trend found in this paper for the austenite proportion has been reported for electro-discharge-machined steel samples [27]. In addition, the different percentages of carbides observed by CEMS and XRD, because of the different depths probed, reveal that the carbides are formed mainly on the surface of the melt pool, while austenite forms mainly at the bottom (see Tables 2 and 3 and Fig. 5).

Some hints as to how these carbides of such diverse compositions are formed, might be obtained examining the Fe-C phase diagram [28], where the temperature of

the solubility line of graphite in the liquid can be seen to grow with carbon concentration. It might occur that because the sample attains higher temperatures in the melted layer, that is deeper when more energetic sparks are used, more carbon may be incorporated into the sample. In the ensuing drastic cooling, the material would reach a zone of the diagram where many different carbides can appear when the concentration is higher than 0.8 at.%, but only austenite and α-Fe would be formed if the rapid cooling finds the material in the region of lower carbon concentration. This carbon concentration line might be connected with the ≈ 0.5 J limit of the current results. The present results are too scant to allow for more elaborate explanations.

4. Conclusions

Carbon containing phases have been found to form after erosion with electric sparks in an organic dielectric. The inclusion of carbon coming from the dielectric into the original α-Fe takes place in a very short time leading to phases out of equilibrium. Austenite and ε-carbide have been found to be formed at energies lower than ca. 0.5 J. Carbides of composition richer in carbon are observed for higher energies.

Acknowledgements

Partial economic support by CONICET (PIP 4326 and PIA 7102), ANPCyT (PICT 1135 and 1277), CICPBA, and Departamento de Materiales, Comisión Nacional de Energía Atómica, Argentina, is acknowledged. The help of Raúl Viña with the X-ray diffraction analyses, that were carried out in the LANADI facilities at La Plata, is thankfully acknowledged. The authors are members of CONICET, Argentina.

References

[1] E.D. Cabanillas, J. Desimoni, G. Punte, R.C. Mercader, J. Appl. Phys. 78 (1995) 2372.
[2] H.K. Lloyd, R.H. Warren, J. Iron Steel Inst. 203 (1965) 238.
[3] L.C. Lim, L.C. Lee, Y.S. Wong, H.H. Lu, Mat. Sci. Tech. 7 (1991) 239.
[4] G.R. Wilms, J.B. Wade, Metallurgia 54 (1956) 263.
[5] H. Opitz, Met. Treat. Drop. Forging 27 (1960) 237.
[6] L. Massarelli, M. Marchionni, Metals Tech. 4 (1977) 100.
[7] A.G. Mamalis, G.C. Vosniakos, N.M. Vaxevanidis, J. Mech. Work Tech. 15 (1987) 335.
[8] P.A. Jacquet, F. Gaillard, A.R. Weill, Memoires Sci. Rev. Metallurg. 63 (1966) 497.
[9] M. Cole, I.A. Bucklow, C.W.B. Grigson, Brit. J. Appl. Phys. 12 (1961) 296.
[10] ICDD, Powder Diffraction File Sets 1–45, Neston Square Corporated Campus, Pennsylvania, 1995.
[11] NRCC, Metals Crystallographic Data File, Ottawa, 1995.
[12] R.A. Young, A. Skthiver, T.S. Moss, C.O. Paiva-Santos, DBWS-9411, 'PC Program for the Rietveld method of Analysis of X-ray Diffractograms of Polycrystalline Samples', Georgia Institute of Technology, Atlanta, 1994.
[13] M. Ron, in: E.L. Cohen (Eds.), Applications of Mössbauer Spectroscopy, vol. II, Academic Press, New York, 1980, p. 329.
[14] J.M.R. Génin, Metall. Trans. 18A (1987) 1371.
[15] O.N.C. Uwakweh, J. Ph. Bauer, J.M.R. Génin, Metall. Trans. 21A (1990) 589.
[16] G. Le Caer, A. Simon, A. Lorenzo, J.M. Génin, Phys. Stat. Sol. (a) 6 (1971) K97.
[17] J.M. Dubois, G. Le Caer, Acta Metall. 25 (1977) 609.
[18] M.A.E. Merdan, R.D. Arnell, Surf. Eng. 5 (1989) 158.
[19] I.A. Bucklow, M. Cole, Met. Rev. 14 (1969) 103.
[20] J.E. Fuller, Metals Handbook, ninth ed. 16 (1989) 556.
[21] P.T. Eubank, M.K. Patel, M.A. Barrufet, B. Bozkurt, J. Appl. Phys. 73 (1993) 7900.
[22] E.D. Cabanillas, Ph. D. Thesis, Universidad Nacional de La Plata, Argentina, 1997.
[23] T. DebRoy, S.A. David, Rev. Modern Phys. 67 (1995) 85.
[24] S.M. Pandit, K.P. Rajurkar, J. Heat Transfer 105 (1983) 555.
[25] A. Erden, F. Arinç, M. Kögmen, J. Mat. Proc. Manuf. Sci. 4 (1995) 163.
[26] H.J. Goldschmidt, Interstitial Alloys, Butterworths, London, 1967.
[27] J.C. Rebelo, A. Morao Dias, D. Kremer, J.L. Lebrun, J. Mat. Process. Technol. 84 (1998) 90.
[28] H. Okamoto, J. Phase Equilibria 13 (1992) 544.